

# **Nek5000 Simulations on Turbulent Coolant Flow in a Fuel Assembly Experiment**

---

*Framatome/ANL Collaboration for Advancing CFD Tools*

**Mathematics and Computer Science Division**

**About Argonne National Laboratory**

Argonne is a U.S. Department of Energy laboratory managed by UChicago Argonne, LLC under contract DE-AC02-06CH11357. The Laboratory's main facility is outside Chicago, at 9700 South Cass Avenue, Argonne, Illinois 60439. For information about Argonne and its pioneering science and technology programs, see [www.anl.gov](http://www.anl.gov).

**DOCUMENT AVAILABILITY**

**Online Access:** U.S. Department of Energy (DOE) reports produced after 1991 and a growing number of pre-1991 documents are available free at OSTI.GOV (<http://www.osti.gov/>), a service of the US Dept. of Energy's Office of Scientific and Technical Information.

**Reports not in digital format may be purchased by the public from the National Technical Information Service (NTIS):**

U.S. Department of Commerce  
National Technical Information Service  
5301 Shawnee Rd  
Alexandria, VA 22312  
**[www.ntis.gov](http://www.ntis.gov)**  
Phone: (800) 553-NTIS (6847) or (703) 605-6000  
Fax: (703) 605-6900  
Email: **[orders@ntis.gov](mailto:orders@ntis.gov)**

**Reports not in digital format are available to DOE and DOE contractors from the Office of Scientific and Technical Information (OSTI):**

U.S. Department of Energy  
Office of Scientific and Technical Information  
P.O. Box 62  
Oak Ridge, TN 37831-0062  
**[www.osti.gov](http://www.osti.gov)**  
Phone: (865) 576-8401  
Fax: (865) 576-5728  
Email: **[reports@osti.gov](mailto:reports@osti.gov)**

**Disclaimer**

This report was prepared as an account of work sponsored by an agency of the United States Government. Neither the United States Government nor any agency thereof, nor UChicago Argonne, LLC, nor any of their employees or officers, makes any warranty, express or implied, or assumes any legal liability or responsibility for the accuracy, completeness, or usefulness of any information, apparatus, product, or process disclosed, or represents that its use would not infringe privately owned rights. Reference herein to any specific commercial product, process, or service by trade name, trademark, manufacturer, or otherwise, does not necessarily constitute or imply its endorsement, recommendation, or favoring by the United States Government or any agency thereof. The views and opinions of document authors expressed herein do not necessarily state or reflect those of the United States Government or any agency thereof, Argonne National Laboratory, or UChicago Argonne, LLC.

# **Nek5000 Simulations on Turbulent Coolant Flow in a Fuel Assembly Experiment**

---

*Framatome/ANL Collaboration for Advancing CFD Tools*

prepared by  
Vakhtang Makarashvili, Elia Merzari, Aleksandr V. Obabko  
Mathematics and Computer Science Division, Argonne National Laboratory

Haomin Yuan  
Nuclear Engineering Division, Argonne National Laboratory

Kostas Karazis  
Framatome Inc.

February 2018

# Contents

Executive Summary . . . . .	ii
1 Introduction . . . . .	1
2 Methods . . . . .	2
2.1 Nek5000 . . . . .	2
2.2 Flow Conditions and Simulation Setup . . . . .	3
3 Results and Comparison with Experimental Data . . . . .	13
3.1 Balanced Flow . . . . .	13
3.2 Unbalanced Flow . . . . .	20
4 Conclusions . . . . .	24
Acknowledgments . . . . .	25
References . . . . .	27

## Executive Summary

The NEAMS program aims to develop an integrated multi physics simulation capability “pellet to plant” for the design and analysis of future generations of nuclear power plants. In particular, the Reactor Product Line code suite’s multi resolution hierarchy is being designed to ultimately span the full range of length and time scales present in relevant reactor design and safety analyses, as well as scale from desktop to petaflop computing platforms. Flow-induced vibration (FIV) is widespread problem in energy systems because they rely on fluid movement for energy conversion. Vibrating structures may be damaged as fatigue or wear occurs. In particular, nuclear fuel rods and steam generators have been known to suffer from FIV and related failures. Nuclear fuel assemblies are exposed to severe thermal, mechanical, and irradiation loads during operation. Global core and local fuel assembly flow fields often result in flow-induced fuel assembly and fuel rod vibration. When coupled with other factors, the vibration might result in excessive fretting wear of fuel rod cladding, and fuel assembly motions may even contribute to significant power oscillations. This phenomenon and its consequences on operational safety margins in fuel assembly designs are primary concerns for nuclear fuel designers. Understanding the particular set of thermal, mechanical, flow, and radiation conditions to which a fuel assembly is subjected and how the fuel assembly responds dynamically to those conditions are important in assessing operational safety margins, and in determining the risk of excessive wear. The ability to better characterize these factors will also enable further design exploration that can lead to better, safer, and more economically viable designs.

Advanced modeling and simulation based on coupled structural and fluid simulations have the potential to predict FIV in a variety of designs, reducing the need for expensive experimental programs, especially at the design stage. Over the past several years, the Reactor Product Line has developed the integrated multi physics code suite SHARP. The goal of developing such a suite is to perform multi physics neutronics, thermal/fluid, and structural mechanics modeling of the components inside the full reactor core or portions of it with a user-specified fidelity. In particular, SHARP contains high-fidelity single-physics codes for structural mechanics (Diablo) and for fluid mechanics calculations (Nek5000). Both codes are state-of-the-art, highly scalable tools that have been extensively validated. These tools form a strong basis on which to build an FIV modeling capability.

In the present report we discuss part of the efforts in the past three years toward the development of this capability and its demonstration on a state-of-the-art fuel assembly experiment. We focus on the validation of the fluid dynamic simulation with Nek5000. The work is performed collaboratively with Framatome, which provided the experimental data for comparison. Numerical simulation results are compared with experimental averages and root mean squares of the velocity demonstrating that Nek5000 can reproduce the flow field in this geometry with reasonable accuracy.

# 1 Introduction

Nuclear fuel assemblies are exposed to severe thermal, mechanical, and irradiation loads during operation. Global core and local fuel assembly flow fields often result in flow-induced vibration (FIV) within fuel assemblies. The cost of inadequate prediction of FIV phenomena within fuel assemblies can be high, since FIV may cause fuel failure and require extensive unit downtime. Hence, the study of FIV is of interest to nearly all vendors and for nearly all reactor designs. While empirical design methods and experience related to FIV might be adequately developed for typical geometries, design methods and experience related to FIV are far less developed for advanced fuel designs such as those planned for advanced reactors or for radical new grid spacer designs. As a result, numerical simulation or analytical prediction of FIV is increasingly important.

The focus of this work is the development of a high-fidelity, finite-element analysis/computational fluid dynamics (FEA/CFD) capability for the simulation of FIV. An advanced numerical simulation capability for modeling FIV phenomena will help improve the analysis and evaluation of different design variants in terms of vibrations and heat transfer performance. Such a capability will complement expensive experimental tests and reduce their cost, while providing a better understanding of the physics behind FIV. Work performed in the previous three years led to the development of such a tool in the multi physics suite SHARP. One-way coupled calculations have been successfully performed for helical steam generators with this tool using Nek5000 and Diablo, the CFD and structural mechanics components of SHARP, respectively [1, 2].

We describe here the simulation of a state-of-the-art fuel assembly experiment performed by Framatome, designed to assess fluid loads on a 5 by 5 rod bundle with grid spacers at various inlet conditions. We focus on the CFD side, since the fluid loads represent the highest uncertainty in the problem and they can be considered as an input to structural calculations in the turbulent fretting regime. Simulation runs were performed on Argonne’s supercomputer Mira, an IBM Blue Gene/Q architecture with 49,152 nodes (16 cores per node) at the Argonne Leadership Computing Facility.

Two cases of flow geometry were simulated with Nek5000 [3]: balanced and unbalanced. In the balanced flow the coolant enters the fuel rod assembly through 121 uniformly spaced inlet holes arranged in an 11x11 matrix. The unbalanced case, on the other hand, features 14 larger holes placed on only one side of the horizontal plane. The simulations were performed in three phases. The initial phase involved testing and adjusting both meshes while decreasing the viscosity to match the target Reynolds number of the physical flow. The second phase involved running simulations long enough to achieve steady-state turbulent flow throughout the entire domain. The third phase involved production runs that collected statistics of three velocity components and pressure. The results were plotted by using the visualization software VisIt, and post processing and analyses were performed in Matlab.

We present here a detailed comparison between the numerical results and experimental data. The results show reasonable agreement between simulations and experiment, representing an important step toward validation of Nek5000 as a simulation capability for FIV studies.

## 2 Methods

### 2.1 Nek5000

The open-source fluid/thermal simulation code Nek5000 is designed specifically for transitional and turbulent flows in complex domains. Nek5000 is based on the spectral element method (SEM) [4], a high-order weighted residual technique that combines the geometric flexibility of finite elements with the rapid convergence and tensor-product efficiencies of global spectral methods. Globally, the SEM is based on a decomposition of the domain into  $E$  smaller subdomains (elements), which are assumed to be curvilinear hexahedra (bricks) that conform to the domain boundaries. Locally, functions within each element are expanded as  $N^{th}$ -order polynomials cast in tensor-product form, which allows differential operators on  $N^3$  gridpoints per element to be evaluated with only  $O(N^4)$  work and  $O(N^3)$  storage.

The principal advantage of the spectral-element method is that convergence is exponential in  $N$ , which implies that significantly fewer gridpoints per wavelength are required to accurately propagate a signal (or turbulent structure) over the extended times associated with high Reynolds number flow simulations. A high-order code involves slightly more work per gridpoint but not more memory access. We emphasize that the reduction in the number of gridpoints is a function of the discretization choice, independent of the implementation; the savings is realized by having an efficient SEM code that does not lead to increased cost per gridpoint.

In addition to its high-order foundation, Nek5000 has several other features. It supports two formulations for spatial discretization. The first is the  $\mathbb{P}_N - \mathbb{P}_{N-2}$  method [5, 6, 7], in which velocity and pressure spaces are represented as tensor-product polynomials of degree  $N$  and  $N - 2$ , respectively, in the reference element  $\hat{\Omega} := [-1, 1]^d$ , where  $d = 2$  or  $3$ .  $E$  elements of the spatial domain consists of the union of elements  $\Omega^e$ , which are parametrically mapped from  $\hat{\Omega}$  to yield a body-conforming mesh. The second is the low-Mach number formulation [8, 9], which uses  $N$ -order approximation spaces for both the velocity and pressure. Temporal discretization is based on a high-order splitting that is third-order accurate in time and reduces the coupled velocity-pressure Stokes problem to four independent elliptic solves per timestep: one for each velocity component and one for the pressure. The velocity problems are diagonally dominant and thus easily solved by using Jacobi-preconditioned conjugate gradient iteration. The pressure substep requires a Poisson solve at each step, which is effected through multigrid-preconditioned GMRES iteration coupled with temporal projection to find an optimal initial guess. Particularly important components of Nek5000 are its scalable coarse-grid solvers that are central to parallel multigrid. The code features a fast direct solver that is optimal up to processor counts of  $P \approx 10^4$  and fast algebraic multigrid (AMG) for  $P \approx 10^5$  and beyond. Counts of 15 GMRES iterations per timestep for billion-gridpoint problems are typical with the current pressure solver.

Nek5000 scales extremely well on the IBM Blue Gene/P and Blue Gene/Q architectures. The code realizes excellent strong scaling, sustaining 60% parallel efficiency with as few as 2,000 points per process for  $P = 1,048,576$ . Typically, production runs have 5,000 - 10,000 points per process and thus run at higher parallel efficiencies.

The approach used to simulate turbulence in the present work is Large Eddy Simulation (LES), with an explicit filter that mimics the deconvolution method [10]. In LES, large-scale turbulence is simulated while smaller scales are modeled. Since smaller scales have a nearly universal behaviour,

LES is a more reliable methodology than is Reynolds-averaged Navier-Stokes, in the sense that it generally depends less on the modelling assumptions. Nek5000 has been validated extensively both in Direct Numerical Simulation (DNS) and LES mode [11, 12].

## 2.2 Flow Conditions and Simulation Setup

### Given Flow Conditions

The experimental geometry consists of a square prismatic section that includes the 5x5 spacer grid and fuel rods. The coolant flow comes from the bottom through numerous holes located below the fuel rods. Two configurations of the flow are considered: (1) balanced flow, where the coolant comes through 121 uniformly spaced holes distributed in an 11x11 matrix, and (2) unbalanced flow, where the fluid flows through 14 larger holes located only one side of the horizontal plane. Three-dimensional models of the balanced and unbalanced flow configurations are given in Figures 1 and 2, respectively.

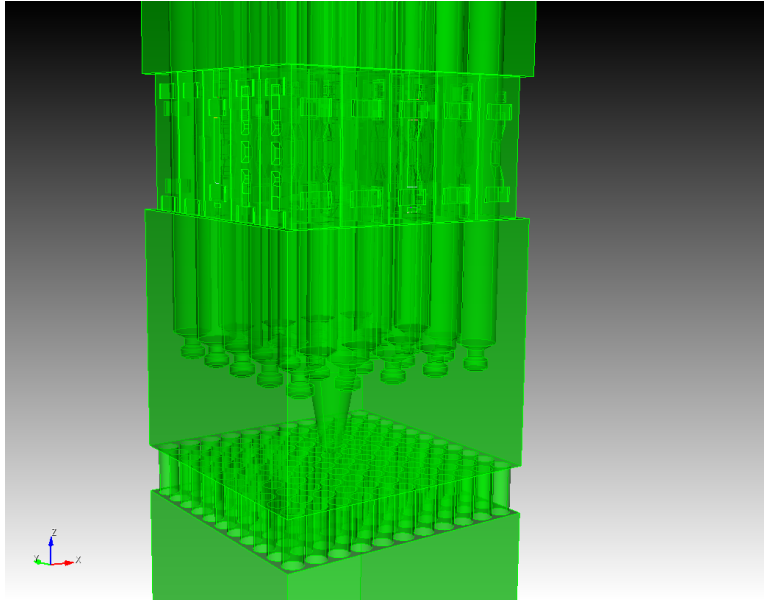


Figure 1: 3D model for the balanced flow geometry.

The orientation of the spacer grid relative to the flow is a critical component of the validation process because of the asymmetric design features. We note that the coordinate system used in the CAD model and subsequently in the Nek5000 simulations (referred to here as “new” -  $XYZ$ ) is different from the coordinate system adopted in the experimental description document (“old” -  $X'Y'Z'$ ). We use only the new coordinate system throughout this report. One needs to apply the following transformation rule to go from the old system to the new.



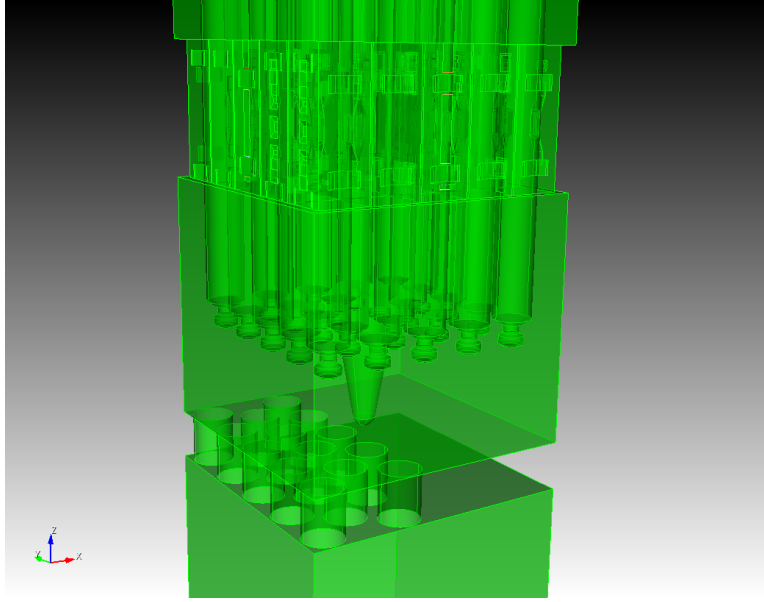


Figure 2: 3D model for the unbalanced flow configuration.

$$X' \rightarrow Z \quad (1)$$

$$Y' \rightarrow -Y \quad (2)$$

$$Z' \rightarrow -X \quad (3)$$

A 2D slice of the spacer grid in the new coordinate system is shown in Figure 3. This Figure makes clear the orientation of the grid in the new system and reveals some of the most complicated asymmetric features of this geometry. The rows of the fuel rods are numbered from 1 to 5 (from the bottom), and the columns are denoted A through E (from the left). The rods B2 and B4 are marked in the figure. These rods are identified because the experimental data were collected on points around these rods — B4 for the balanced flow and both B2 and B4 for the unbalanced flow.

The numbering scheme of the experimental data points was identical for B2 and B4 and is illustrated in Figure 4. The circle represents either pin B2 or pin B4. The length  $a$  is half of the distance between the centers of the neighbouring rods — A2, B1 for B2 and A4, B3 for B4 — and equals 0.63 in nondimensional units (i.e., normalized per reference length scale,  $L$ ). All values in this report are given in nondimensional units. Point 7 for both rods is located in the middle of the subchannel formed by rods A1-B1-A2-B2 and A3-B3-A4-B4, accordingly. Points 2 and 4 are located at 0.03 from the corresponding rod surfaces. Point 6 is 0.1 away from the rod surface, while point 5 is equidistant between points 4 and 7. Instantaneous raw numerical data for three velocity components and pressure were collected from Nek5000 simulations at points 1, 2, 4, 5, 6, 7, and 9 for both flow configurations.

Experimental data were collected at four different elevations measured from the bottom ( $Z_{min}$ ) for the points defined above. Both flow geometries for the CFD simulations were truncated in order to make computations feasible and included only a small region beyond the last experimental plane.

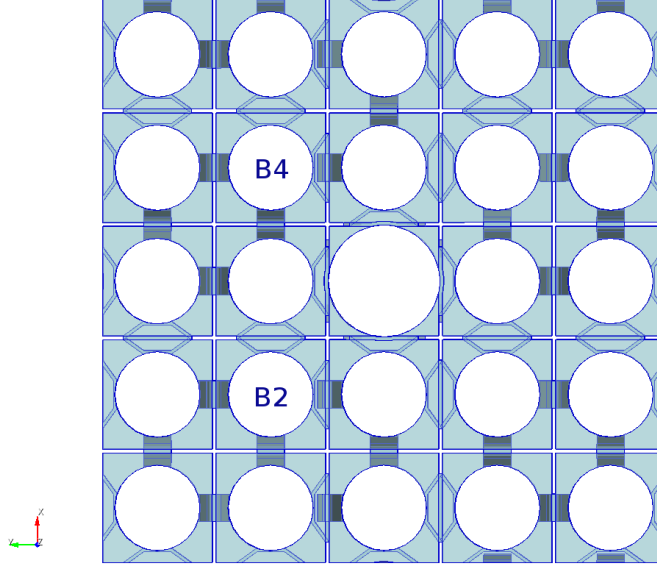


Figure 3: Top view of the spacer grid -  $XY$  plane depicting a  $5 \times 5$  rod bundle matrix and intricate geometry details between the rods.

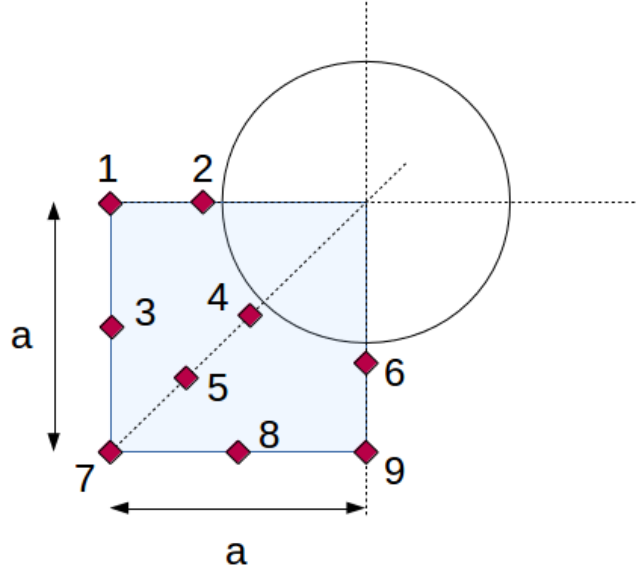


Figure 4: Numbering convention of the experimental data points around the rods B2 and B4.

Two elevations were below the spacer grid and two above. These locations are given in Table 1.

Thus, raw numerical results of the entire flow history were recorded for 28 points for the balanced case (4 elevations and 7  $XY$  points for the rod B4) and 56 points for the unbalanced case

Table 1: Numerical results of the flow history recorded at these four elevations measured from the bottom ( $Z_{min}$ ) and presented as a percentage of the model height.

<b>Location</b>	<b>Z coordinate</b> [% of Height]
H1	33.5
H2	42.5
N1	69.5
N2	90.5

Table 2: Fluid properties and flow characteristic used in simulations.

<b>Density</b> [ $kg/m^3$ ]	<b>Dynamic Viscosity</b> [ $kg/m/s$ ]	<b>Mean Velocity</b> [ $m/s$ ]
1840	1.4168E-03	2

(additional 28 points for the rod B2). Fluid properties and flow characteristics used in both the balanced and unbalanced flow simulations are given in Table 2.

Nek5000 simulations were carried out in a nondimensional form using the reference length scale  $L$  and the reference velocity scale  $U$  to rescale the length, velocity and time using the following simple transformations:

$$l^* = \frac{l}{L} \quad (4)$$

$$u^* = \frac{u}{U} \quad (5)$$

$$t^* = \frac{l^*}{u^*} = \frac{t}{L/U} \quad (6)$$

where  $l^*$ ,  $u^*$  and  $t^*$  are nondimensional length, velocity, and time, respectively.

We chose the rod diameter as the reference length scale. The velocity reference scale, on the other hand, was set to the inlet velocity that would result in a mean flow velocity of 2 m/s. The Reynolds number of the flow based on the rod diameter and the inlet velocity was then found to be

$$Re = \frac{LU}{\nu} \approx 15,000, \quad (7)$$

where  $\nu$  denotes the kinematic viscosity (dynamic viscosity divided by density -  $\mu/\rho$ ) and is calculated according to the values in Table 2.

## Mesh and Nek5000 Setup

By far the most challenging and time-consuming part of this simulation project was building a working computational mesh for both the balanced and unbalanced flow cases. The project went

through multiple iterations of mesh building, testing, identifying problematic regions, and adjusting and rebuilding phases. Almost all the complications were caused by the spacer grid region, where many small and intricate geometric features made building a hexahedral (hex) mesh from scratch infeasible. Were it not for the spacer grid region, the rest of the geometry would have been trivial to mesh. A successful and practical meshing strategy turned out to be using the automatic tetrahedral (tet) meshing capability of ANSYS ICEM software and then converting a tet mesh into a hex mesh by splitting each tet element into four hex elements. The geometry was first meshed between  $z \in [-10, 2.5]$  and then extruded below  $z = -10$  and above  $z = 2.5$ . The hardest part of this process was making sure that the initial tet mesh was properly projected to the CAD geometry and then adding thin boundary layers around the fuel pins and the outer walls throughout the entire geometry to ensure the accuracy of the results in those areas.

Figure 5 shows  $XZ$  vertical slices (at  $Y = 0$ ) of the final mesh for both the balanced and unbalanced flow geometries. The CAD geometries for both cases were truncated at  $Z = -11$  and  $Z = 9$  in order to transport transient flow features through the entire geometry in a reasonable time, thus making simulations computationally feasible. The mesh for the balanced flow configuration consisted of  $E = 3,415,283$  elements, while the unbalanced flow mesh had  $E = 2,084,165$  elements.

Figure 6 is a close-up version of the same meshes shown in Figure 5, revealing mesh features above the inlet holes for both meshes. One can see from these snapshots how the initial, automatically generated tet elements were later split into hex elements. The figure also shows high element densities around the fuel rods, ensuring adequate resolution in the critical regions of the flow.

Figure 7 shows vertical and horizontal slices of the mesh in the most complicated region of the geometry, the spacer grid. The small and intricate geometric features made building a hex mesh for this region and combining it with the rest of the geometry infeasible. The springs and spacers themselves do not have the boundary layers, but the mesh elements around them are small enough to give a smooth solution and avoid numerical instabilities.

Figure 8 illustrates a horizontal  $XY$  plane of the mesh above the spacer grid. Both flow configurations have almost identical meshes in this portion of the geometry as well. The top part of Figure 8 shows the entire  $5 \times 5$  fuel rod assembly, while the bottom part demonstrates the mesh around a single rod, including a nice thin boundary layer around the rod; this ensures that the results close to the rod surfaces are correct and free of runaway numerical instability problems. The mesh also includes the boundary layers around the square walls of the geometry. Figure 9 shows a comparison between the balanced and unbalanced meshes in the inlet region. These are  $XY$  profiles at  $z = -8$ . The top picture is the balanced mesh of the  $11 \times 11$  inlet holes, while the bottom picture is the mesh of the 14 larger holes on the left side of the unbalanced flow geometry.

After the mesh design was finalized, the next phase of the simulation project was to run both cases long enough to reach a statistically steady turbulent state at the target Reynolds number (see Eq. 9). The balanced case was run to  $t = 7.65$ , while the unbalanced case was run to  $t = 3.73$  in convective time units before acquiring data. All simulations were performed with polynomial order  $N = 7$ , corresponding to a total number of mesh points  $n \approx EN^3 \approx 1.17$  billion and  $n \approx 0.71$  billion for the balanced and unbalanced flow meshes, respectively. All the runs were done with a  $\mathbb{P}_N - \mathbb{P}_{N-2}$  method for spatial discretization. Throughout the entire work, the approach to simulate turbulence was large eddy simulation, with an explicit filter that mimics the deconvolution method. The filtering for the deconvolution LES mode was set to 5% on the last mode for both the balanced and unbalanced flow simulations. The initial conditions at  $t = 0$  were set to  $(v_x, v_y, v_z) = (0, 0, 1)$ . All

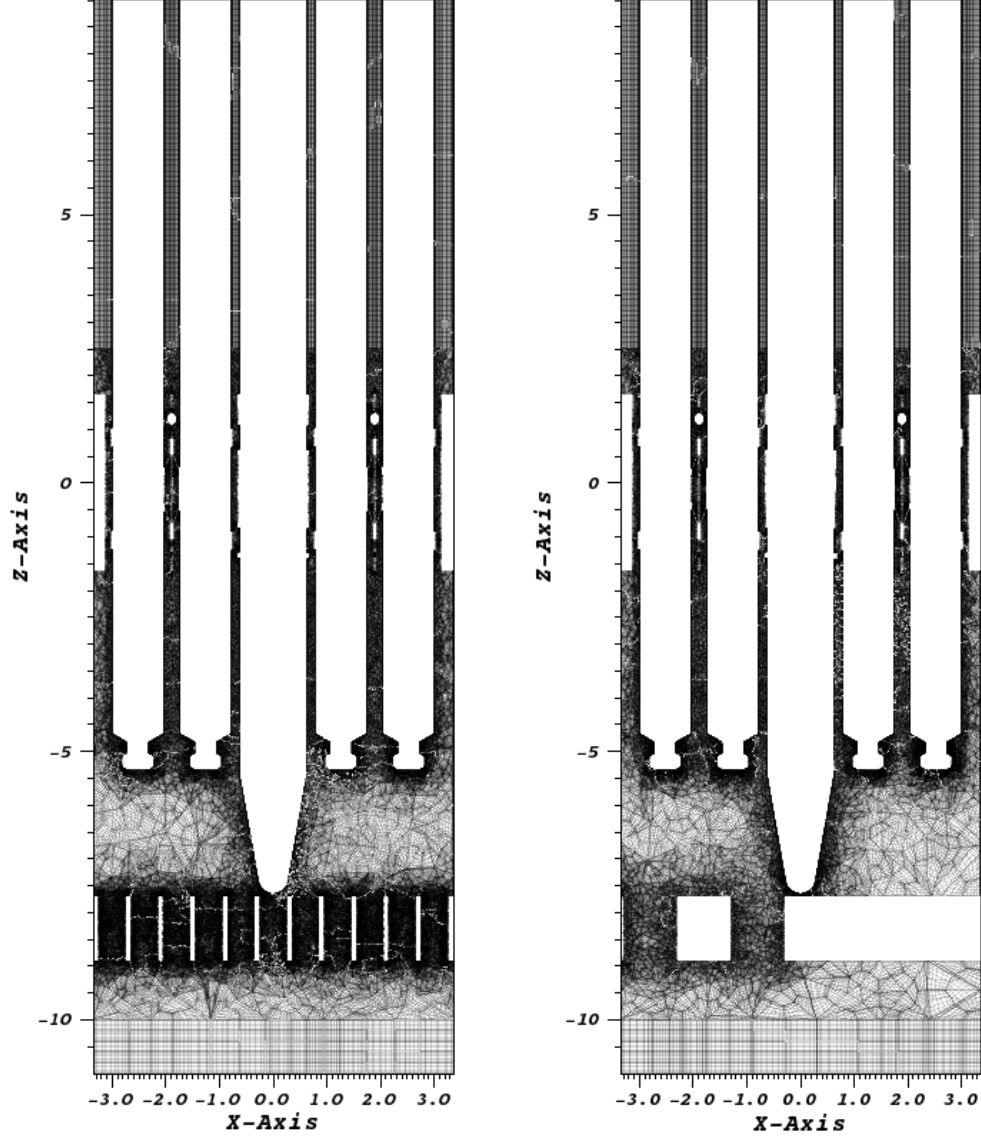


Figure 5: Vertical  $XZ$  profiles of the final computational meshes at  $Y = 0$ . Left: balanced flow geometry; right: unbalanced flow geometry.

subsequent runs were restarted from the velocity field profiles obtained by the previous simulation. The boundary conditions were the following for both flow configurations: inlet boundary at  $z = -11$  with  $(v_x, v_y, v_z) = (0, 0, 1)$ , turbulent outflow at  $z = 9$  and wall boundary conditions at the outer walls and rod surfaces. The timestep was  $\Delta t = 2.5 \cdot 10^{-5}$  in convective units, or about  $2 \cdot 10^{-7}$  seconds for the balanced flow and  $\Delta t = 1.25 \cdot 10^{-5}$  in convective units, or about  $1 \cdot 10^{-7}$  seconds for the unbalanced flow. We used the characteristics time stepping scheme [13] for both flow configurations. This scheme avoids the CFL constraint in the semi implicit formulation by treating the non-linear

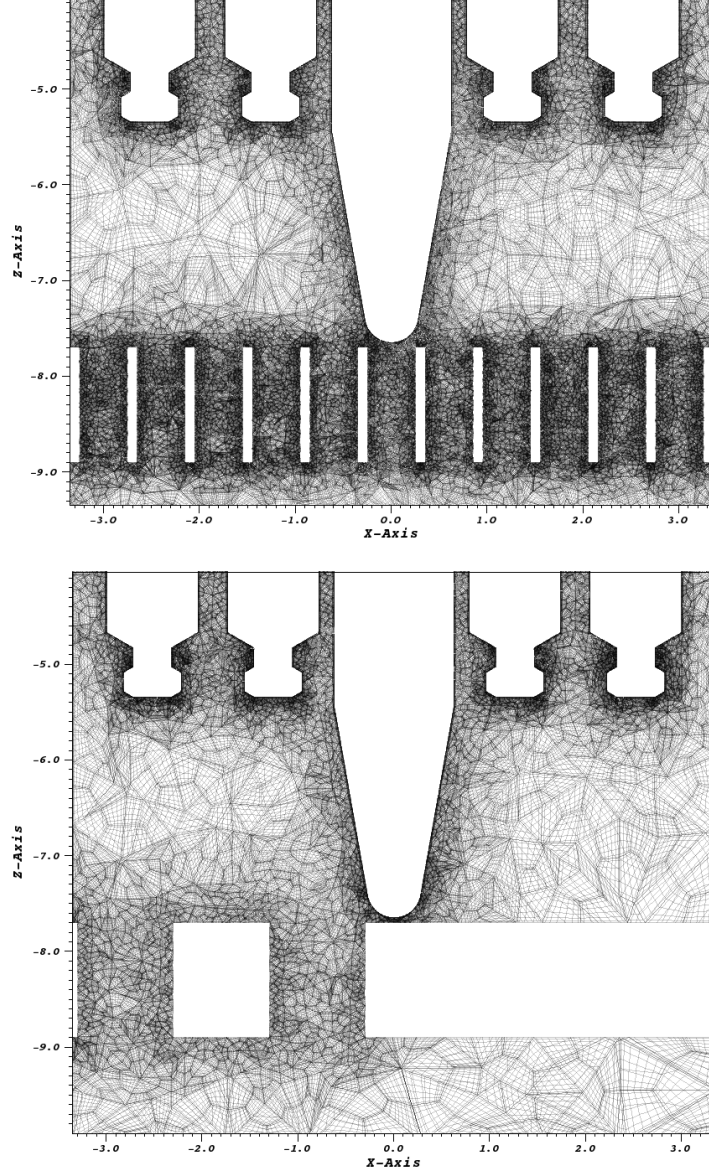


Figure 6: Close-up vertical snapshots of the computational mesh above the inlet holes.  $XZ$  plane at  $Y = 0$ . Top: balanced flow configuration; bottom: unbalanced flow configuration.

convective term in Navier-Stokes as a material derivative which represents the change along the path line (characteristic) associated with the convecting velocity field. This allowed larger timesteps with the CFL in the region of 5-7 for both simulations. The data were collected over the time interval of  $t \in [7.65, 11.6]$  (convective units) and  $t \in [3.73, 4.8]$  for balanced and unbalanced flow simulations, respectively. All the runs were performed on ALCF's supercomputer Mira - an IBM BlueGene/Q system using 8192 compute nodes with 32 MPI ranks per node, totalling 262144 MPI

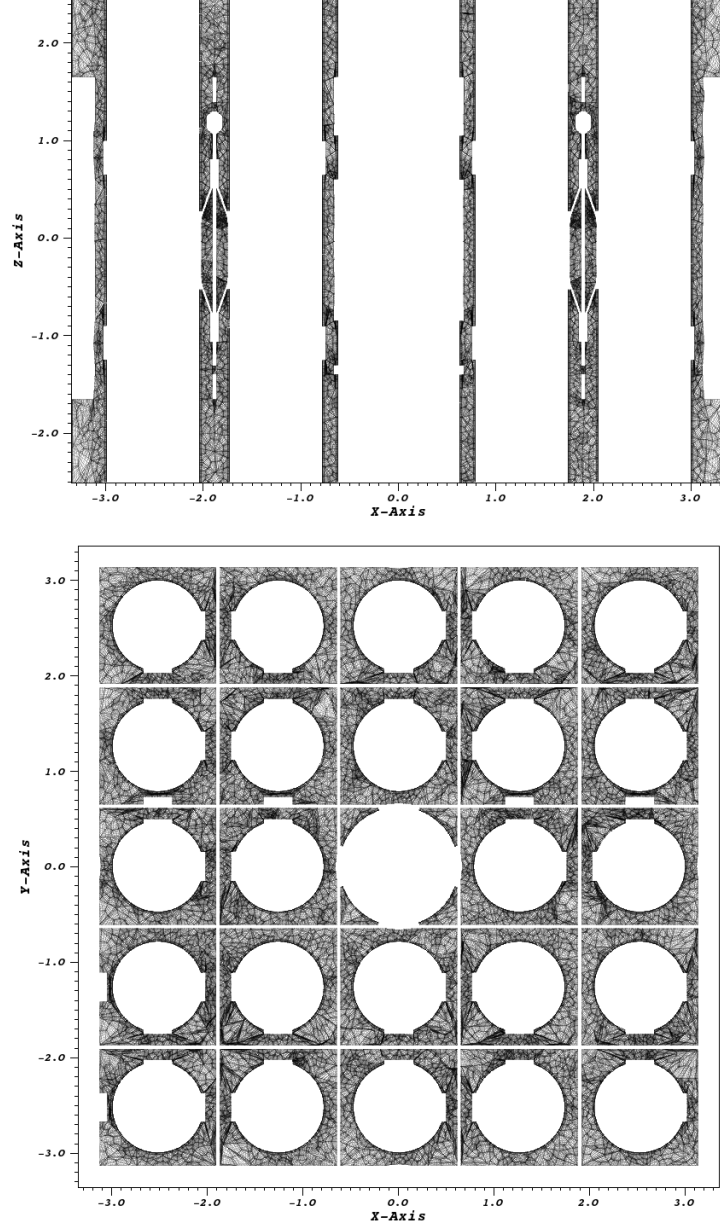


Figure 7: Mesh in the spacer grid region, which is nearly identical for both flow geometries. Top:  $XZ$  slice at  $Y = 0$ ; bottom:  $XY$  slice at  $Z = 0$ .

ranks for each simulation. This allowed excellent strong scaling, sustaining more than 60%-70% parallel efficiency with around 4400 points per process for the balanced case and around 2700 points per process for the unbalanced flow.

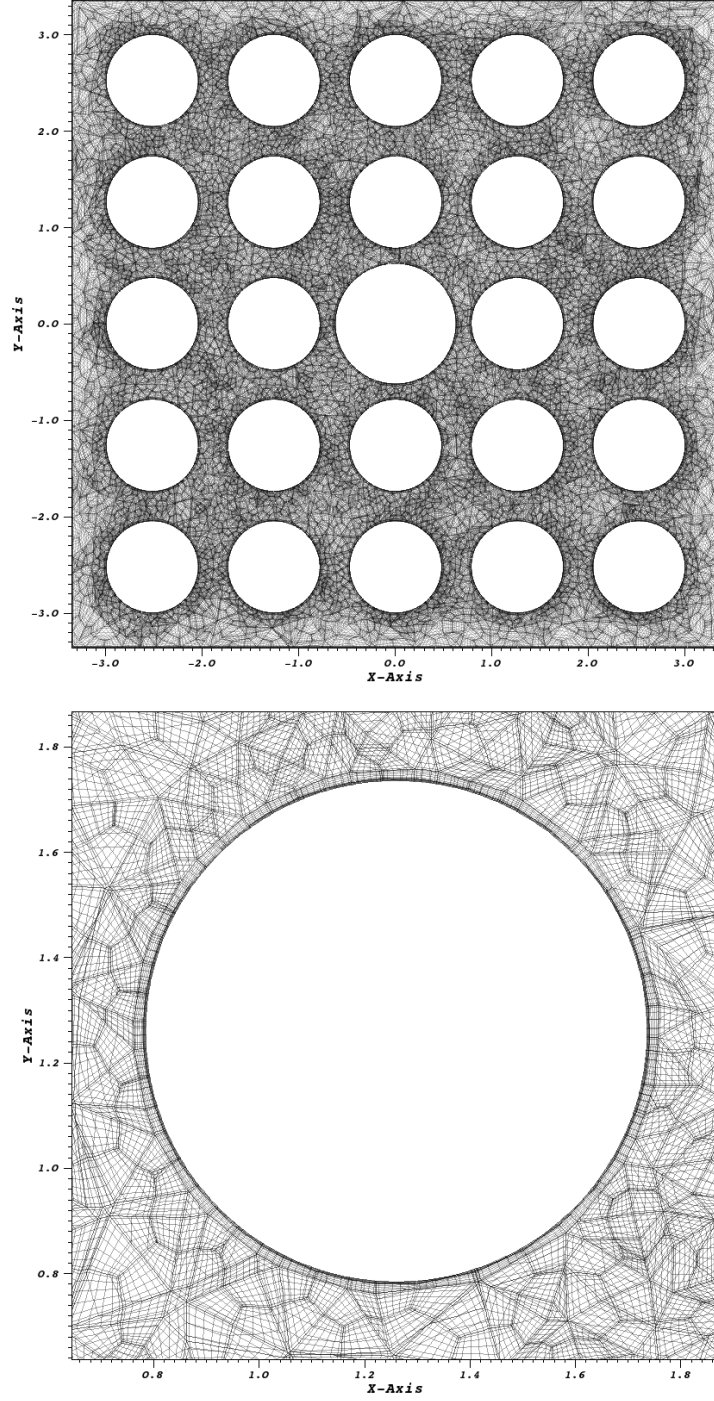


Figure 8: Horizontal  $XY$  profile of the balanced geometry mesh above the spacer grid region. Top: entire  $XY$  plane; bottom: mesh around the B4 fuel rod.



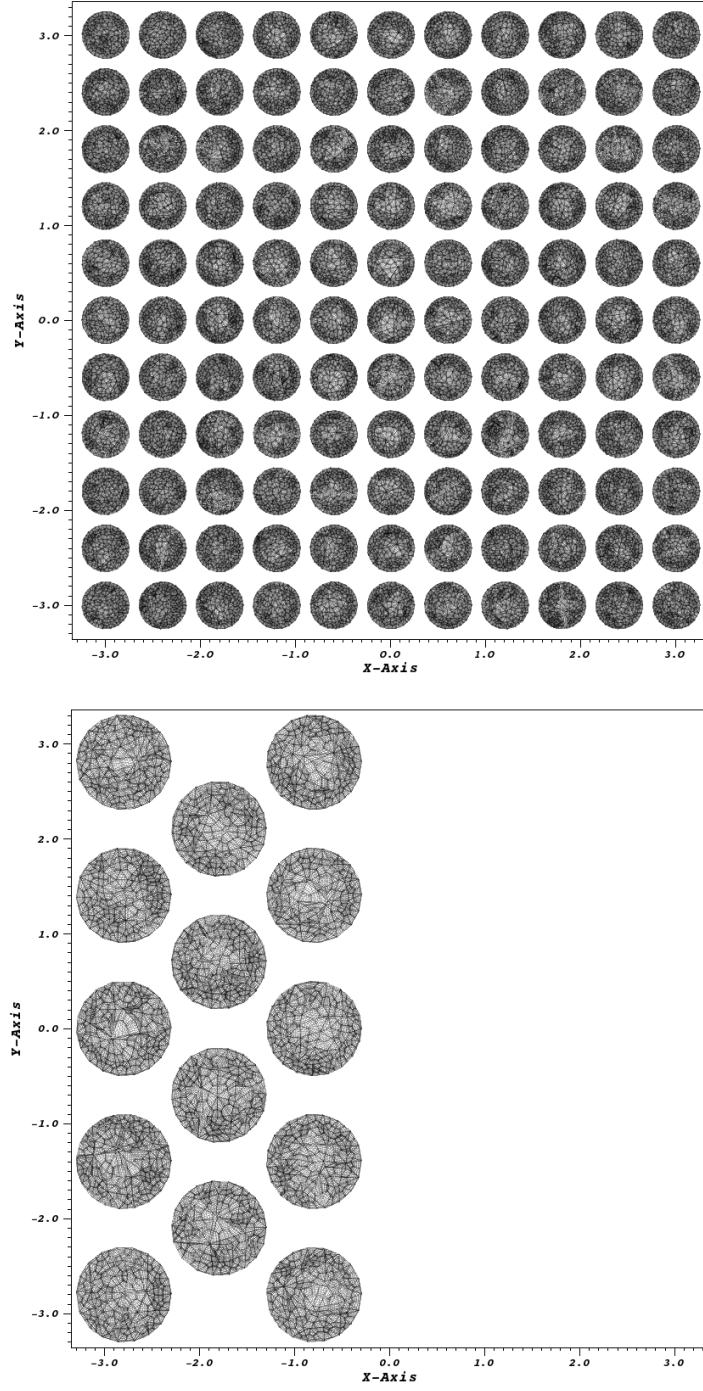


Figure 9:  $XY$  mesh profiles at the inlet -  $Z = -8$ . Top: mesh for the 11x11 inlet holes for the balanced flow; bottom: 14 larger inlet holes of the unbalanced geometry.

### 3 Results and Comparison with Experimental Data

We present here the results for both the balanced and unbalanced flow simulations along with comparison with the experimental data (where available). The results for the balanced case are based on the data collected over four convective time units (corresponding to about 33 ms of physical time) and they exhibit satisfactory statistical convergence. The data for the unbalanced case, on the other hand, were collected only over one convective time unit ( $\approx 8.25$  ms) and should be treated as preliminary. The results can be significantly improved by running the simulation longer in order to collect more statistics. Also, higher accuracy for both cases can be achieved by increasing the polynomial order or adjusting the mesh at certain places that would allow smoother profiles. We note that mesh tuning is a more feasible approach since the increase of polynomial order often proves to be computationally too expensive for meshes of this scale. The next two subsections summarize the major results for each flow configuration.

#### 3.1 Balanced Flow

First, we show some of the profiles of the instantaneous axial velocity,  $w$ . Figure 10 is a vertical  $XZ$  profile of the flow field, while Figures 11 and 12 are two horizontal  $XY$  profiles at H2 (below the spacer grid) and N1 (above the spacer grid), respectively. These plots show the main turbulent features of the axial flow. Figure 10 shows the highly turbulent flow coming through the inlet holes and entering the rod assembly region along with convective acceleration of the flow in the spacer grid. Higher flow velocities can be observed in channels between the rods in Figures 11 and 12, both demonstrating very turbulent axial flows. Time-averaged axial velocity fields for planes N1 and N2 above the spacer grid are given in Figures 13 and 14, respectively. These smooth profiles provide a confirmation of the statistical convergence and reflect the geometric characteristics of the grid. We point out that the color schemes are different on each plot. The blue and the dark red are defined based on the minimum and maximum of each profile, respectively.

Time averages and standard deviations (rms) of the axial flow velocity were calculated for 28 points around the B4 rod based on the data recorded at each timestep over the course of the entire simulation. There were 7 points (1, 2, 4, 5, 6, 7, and 9; see Figure 4) for each of the 4 elevations (H1, H2, N1, and N2. see Table 1). These results were plotted together with the experimental data provided by Framatome. Figure 15 gives the results of average axial velocities (denoted by circles) grouped by points as a function of elevation along with experimental data (marked as x's). The dashed lines are provided to guide the eye for trends. Figures 16 and 17 demonstrate the same results in a different representation. They are grouped for planes H1—H2 and N1—N2, respectively. The squares are the results obtained from the simulation, while x's represent the experimental data points. Figures 15, 16, and 17 demonstrate mostly good agreement between the simulation and experimental results. The points that exhibit worse agreement with the experimental data in general tend to be those that are closer to the rod surface — 2, 4, and 6. Noticeable deviations from the experimental results are visible for points 2 and 4 for H1, only point 2 for H2, and point 6 for planes N1 and N2. We note that points 2 and 4 are close to the rod B4 surface and therefore reside on an edge of a steep gradient curve. A combination of small experimental and simulation discrepancies related to sampling data at these points can easily lead to a significant disagreement. A relatively large discrepancy for point 6 above the grid suggests that experimental and simulation sampling

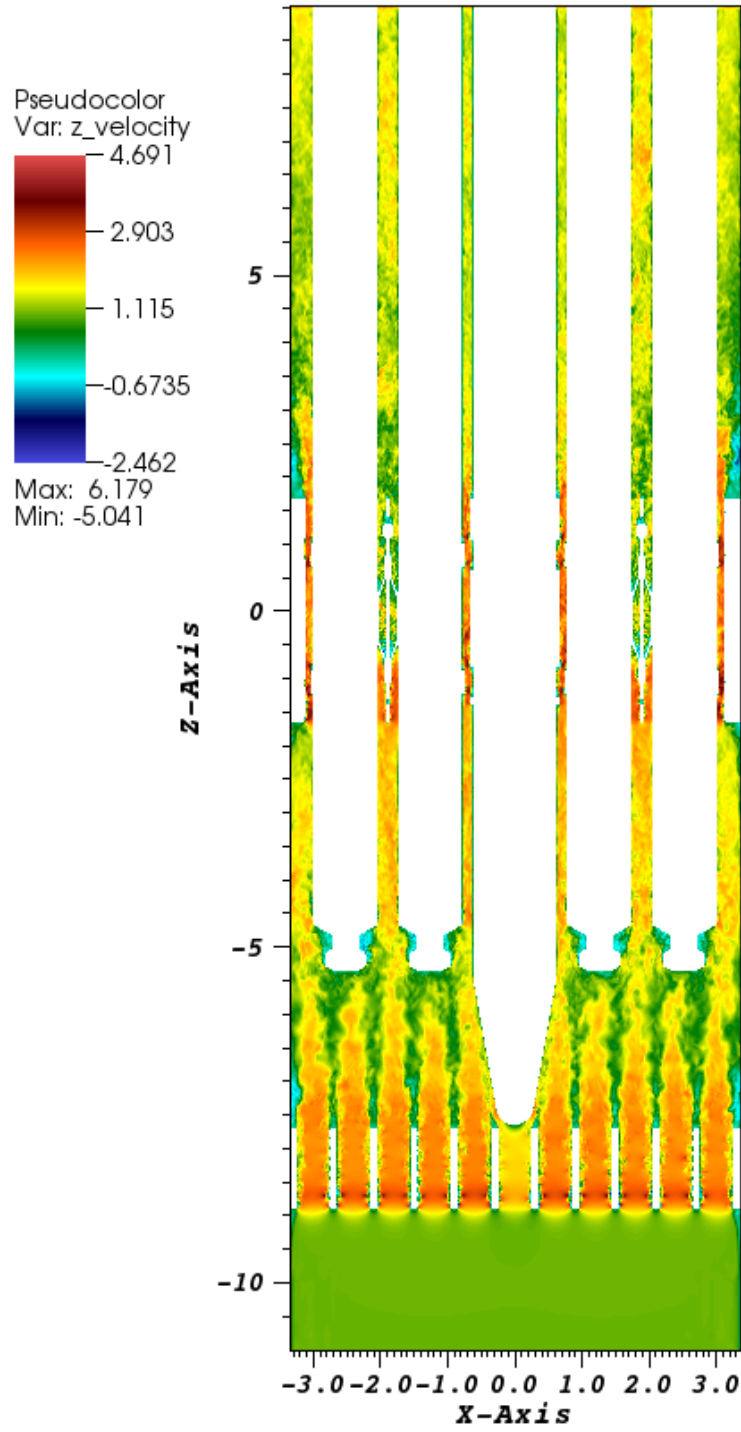


Figure 10: Vertical  $XZ$  profile of the instantaneous axial velocity flow field at  $y = 0$ .

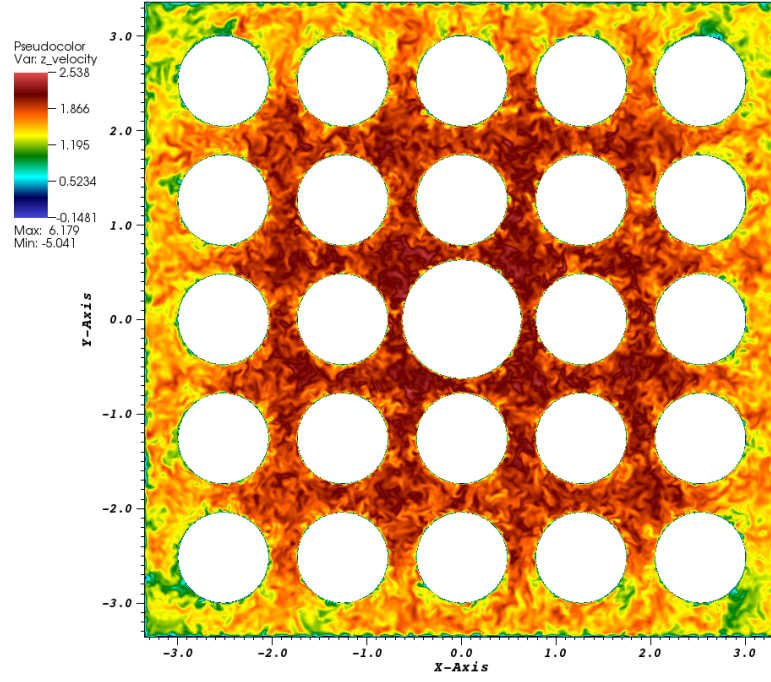


Figure 11: Horizontal  $XY$  profile of the instantaneous axial velocity flow field at H2.

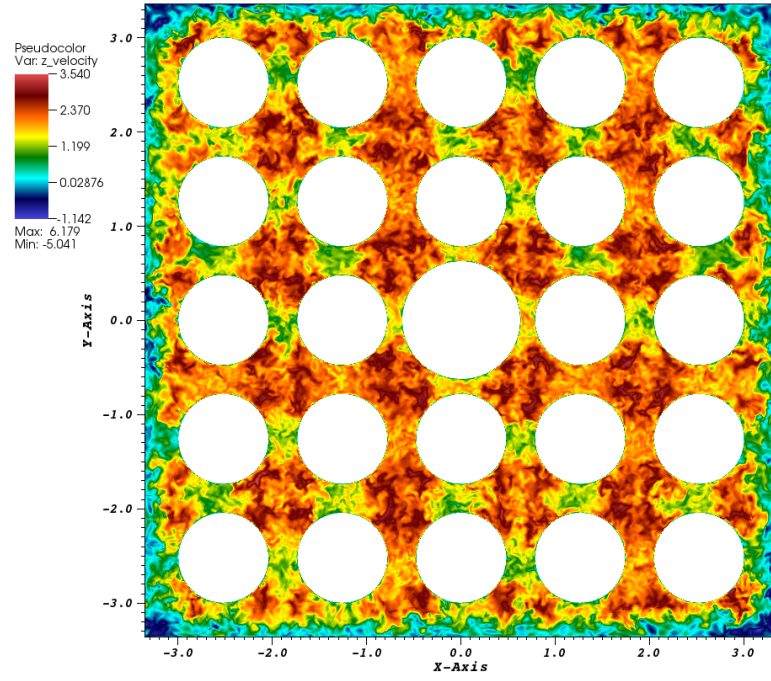


Figure 12: Horizontal  $XY$  profile of the instantaneous axial velocity flow field at N1.

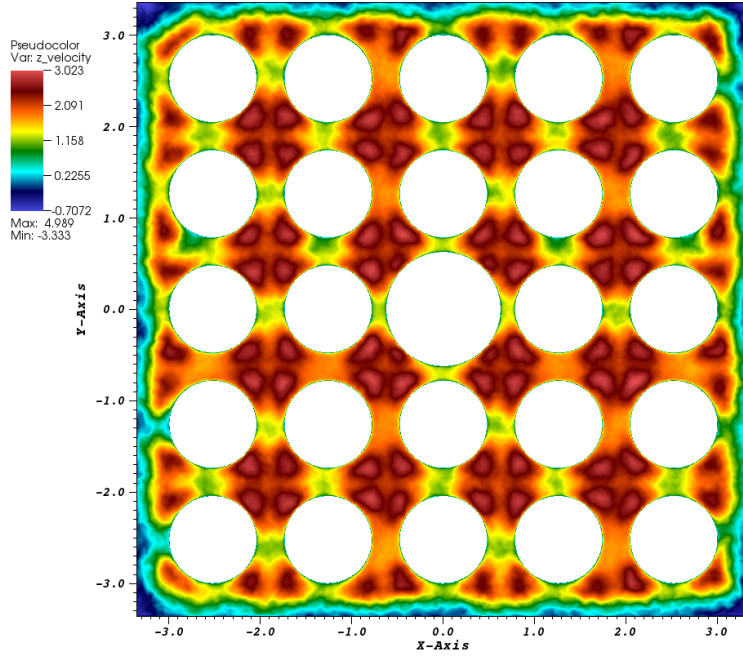


Figure 13: Horizontal  $XY$  profile of the time averaged axial velocity flow field at N1.

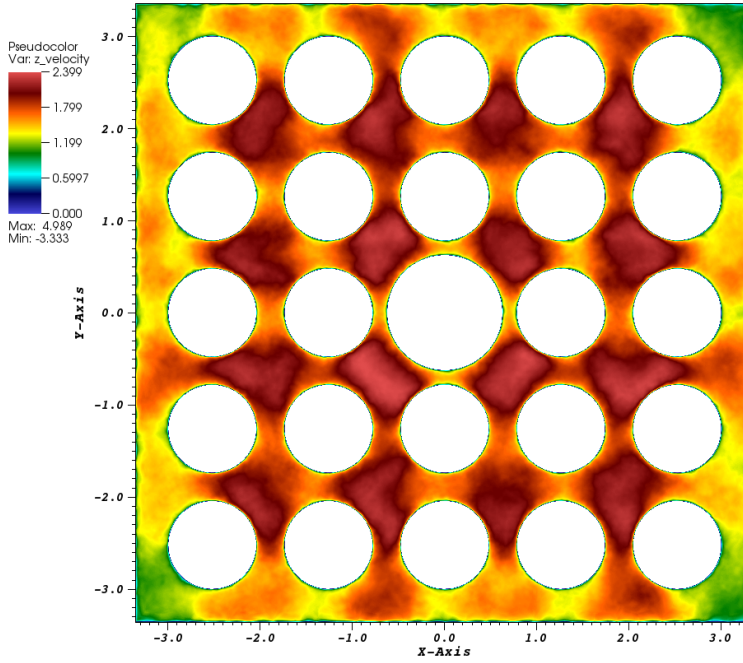


Figure 14: Horizontal  $XY$  profile of the time-averaged axial velocity flow field at N2.

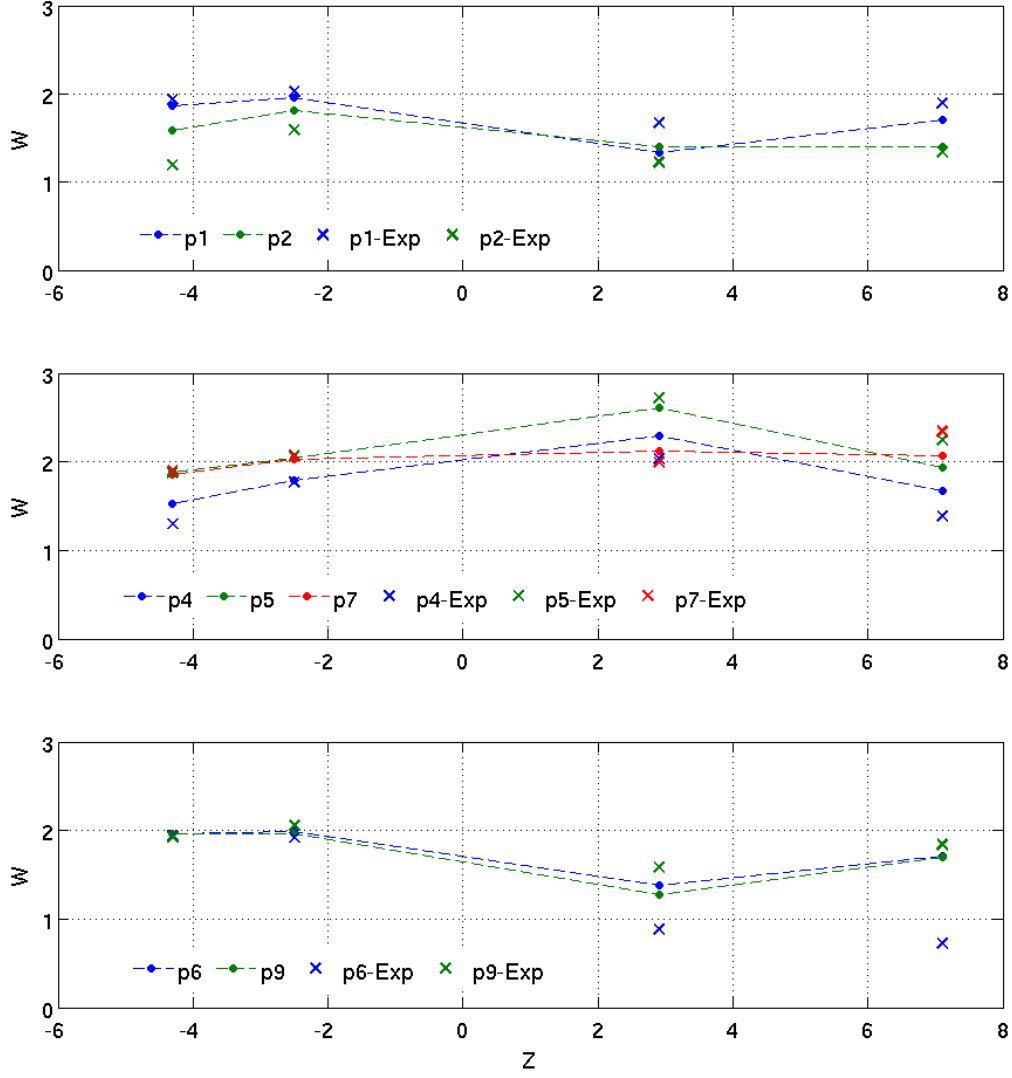


Figure 15: Simulation and experimental values for the average axial velocity  $W$  as a function of the  $Z$  coordinate for all seven points. All values are in convective units.

locations could have been different. The velocity fields are orientation dependent above the grid.

Figures 18 and 19 respectively show calculated turbulent intensity of the axial velocity component compared with the experimental results at elevations H1—H2 and N1—N2. The turbulent intensity for each component is defined as the ratio of the standard deviation (or rms) of the velocity over the mean axial flow velocity. Thus, for the axial component, it would be  $I_w = \sigma_w / \bar{W}$ . These plots also show a similar tendency. Simulated results are mostly in good agreement with the experimental data except for points 2 and 4 for H1 and H2 and points 2, 4, and 6 for planes N1 and N2. The disagreements for points 2 and 4 are more pronounced for turbulent intensity compared with the average values since the standard deviation is a more sensitive quantity.

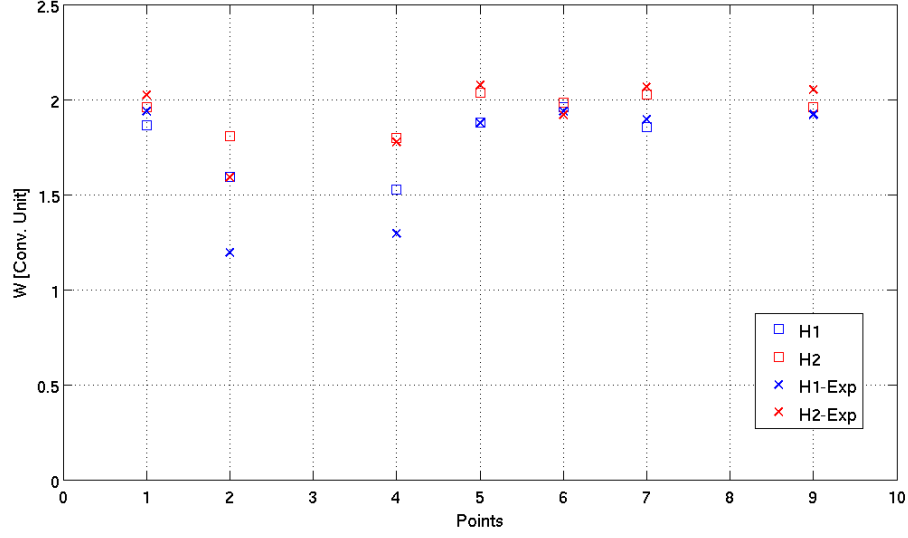


Figure 16: Time-averaged axial velocities compared with experimental results. The values are in nondimensional convective units at the points around the rod B4 for planes H1 and H2.

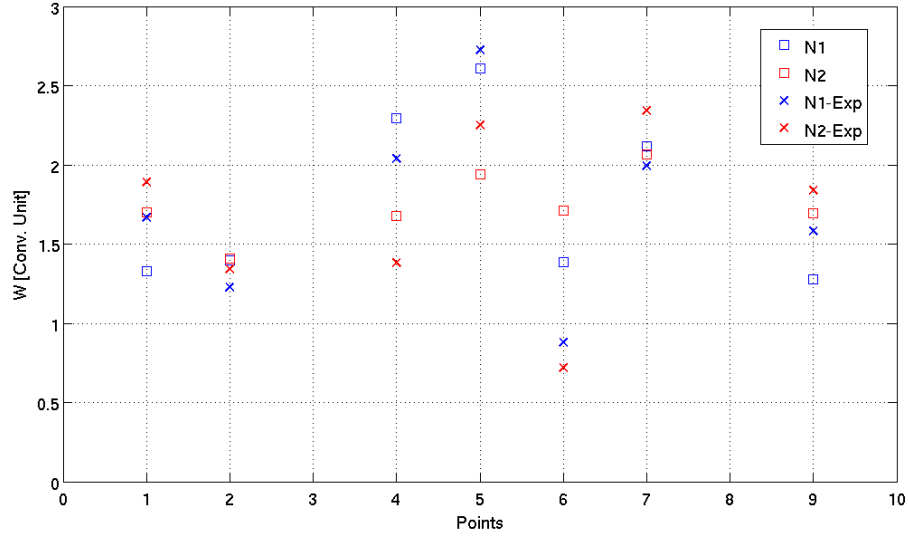


Figure 17: Time-averaged axial velocities compared with experimental results. The values are in nondimensional convective units at the points around the rod B4 for planes N1 and N2.

Besides time averages and turbulent intensities, autocorrelations and Fourier spectra of all three velocity components were also calculated for those points of interest around the rod B4 at all four planes, H1, H2, N1, and N2. Figure 20 shows Fourier spectra of the axial velocity component for all the points at plane H1. The results of the Fourier spectra at the other three planes are similar and are not given here. Shapes of the curves shown in this figure are in a good agreement with the

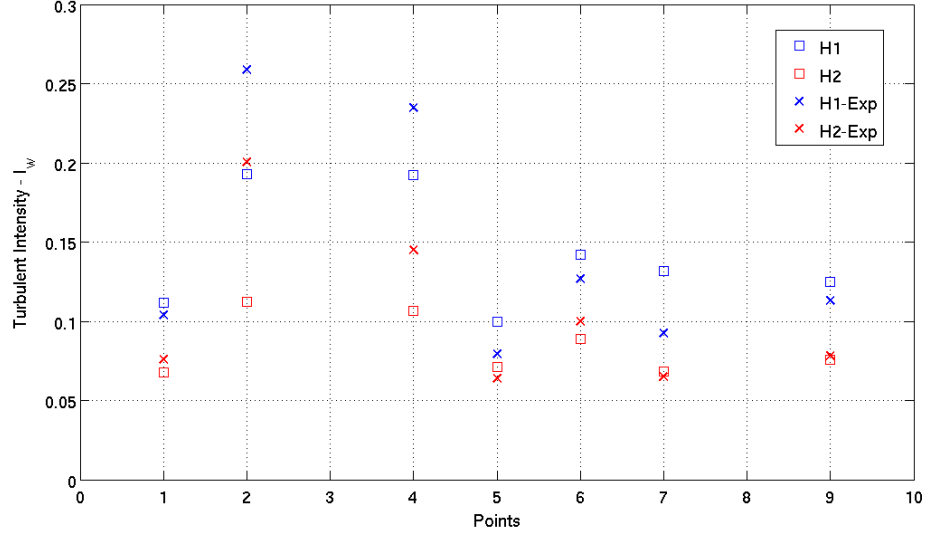


Figure 18: Axial turbulent intensity compared with experimental results. The data is for the points around the rod B4 at elevations H1 and H2.

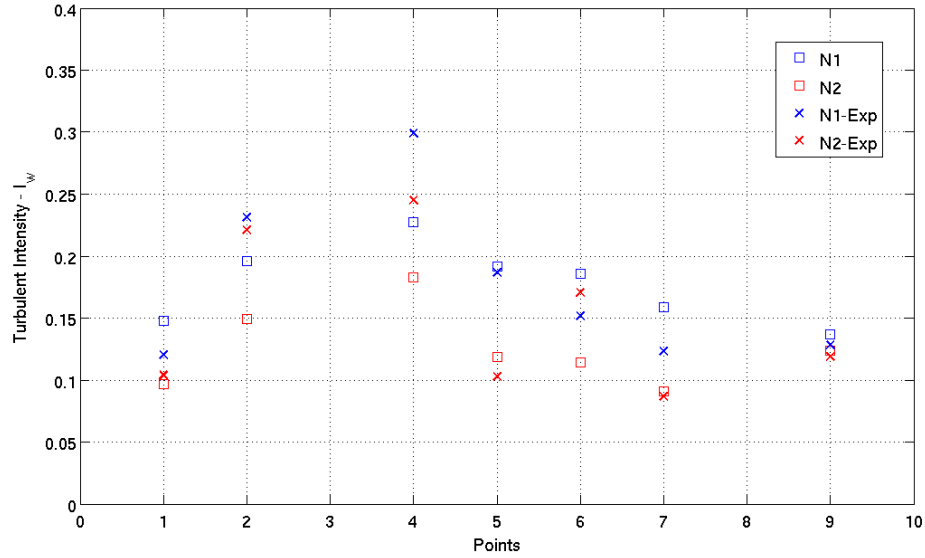


Figure 19: Axial turbulent intensity compared with experimental results. The data is for the points around the rod B4 at elevations N1 and N2.

experimental spectra provided by Framatome. However, more statistics are required spanning a longer period of time in order to obtain smoother spectra and sufficiently resolve the low-frequency region. We have covered only about 33 ms of the physical flow time for the balanced flow simulation.



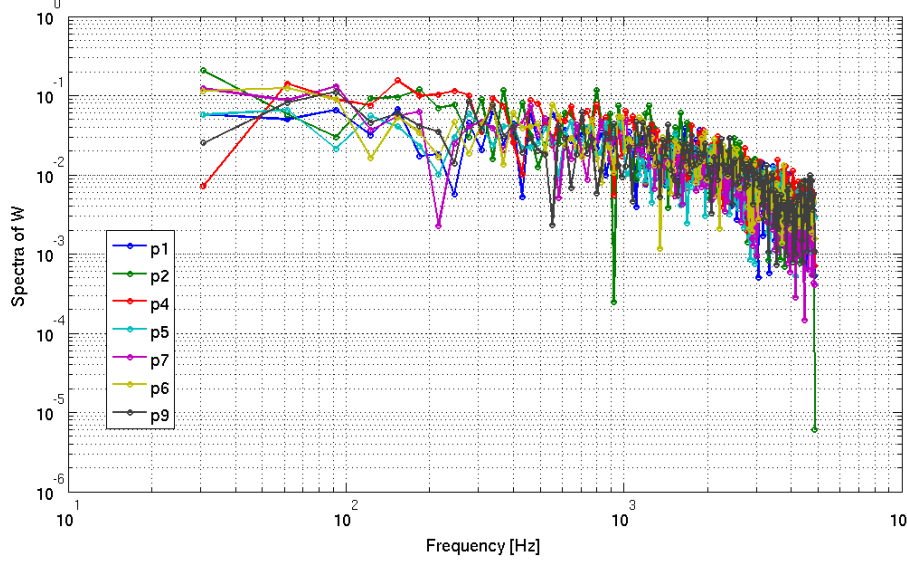


Figure 20: Fourier spectra of the axial velocity component for the seven points around the rod B4 at the plane of H1.

### 3.2 Unbalanced Flow

2D profiles of the instantaneous axial velocity -  $w$  are presented here. Figure 21 is a vertical  $XZ$  profile of the axial flow, while Figures 22 and 23 are two horizontal  $XY$  profiles at H1 and N1, respectively. These plots are also a good demonstration of the main turbulent characteristics of the axial flow. Figure 21 clearly shows the unbalanced (i.e., nonuniform across  $XY$ ) turbulent flow coming through the one-sided inlet holes on the left and entering the rod assembly region along with the recirculation region on the right side of the central rod. Figure 22 shows uneven axial velocity distributions in the channels between the rods below the spacer grid at H1, while Figure 23 shows a similar plot above the spacer grid at N1. Again, the color schemes are different on each plot.

Time averages and standard deviations of the axial flow velocity were calculated for 56 points — 28 points around the rod B2 and another 28 points around B4. The data were recorded at each timestep over the entire time domain of the simulation. These results were plotted together with the experimental data provided by Framatome. Figure 24 compares results of the mean axial velocity  $W$  at those 7 points for rods B2 and B4 along with the experimental values at the plane N1 above the grid spacer. Figure 25 shows similar results for the rod B4 at planes H2 and N2 and a comparison with the experimental data. As with the balanced case, squares are the results obtained from the Nek5000 simulation, while x's represent the experimental data points. The plots show that the agreement with the experiment and in general quality of the results are considerably worse for the unbalanced case than for the balanced one. The main contributor to this inconsistency is the lack of adequate statistical convergence. Acquiring more data will improve results significantly. The worst agreement is for the points 1, 5, and 9 for plane N1 on Figure 24, while points 2 and 4 show the most pronounced disagreement (the same trend that was observed for the balanced case) for plane H2 on Figure 25. Overall, these plots show somewhat reasonable agreement with the experiment.

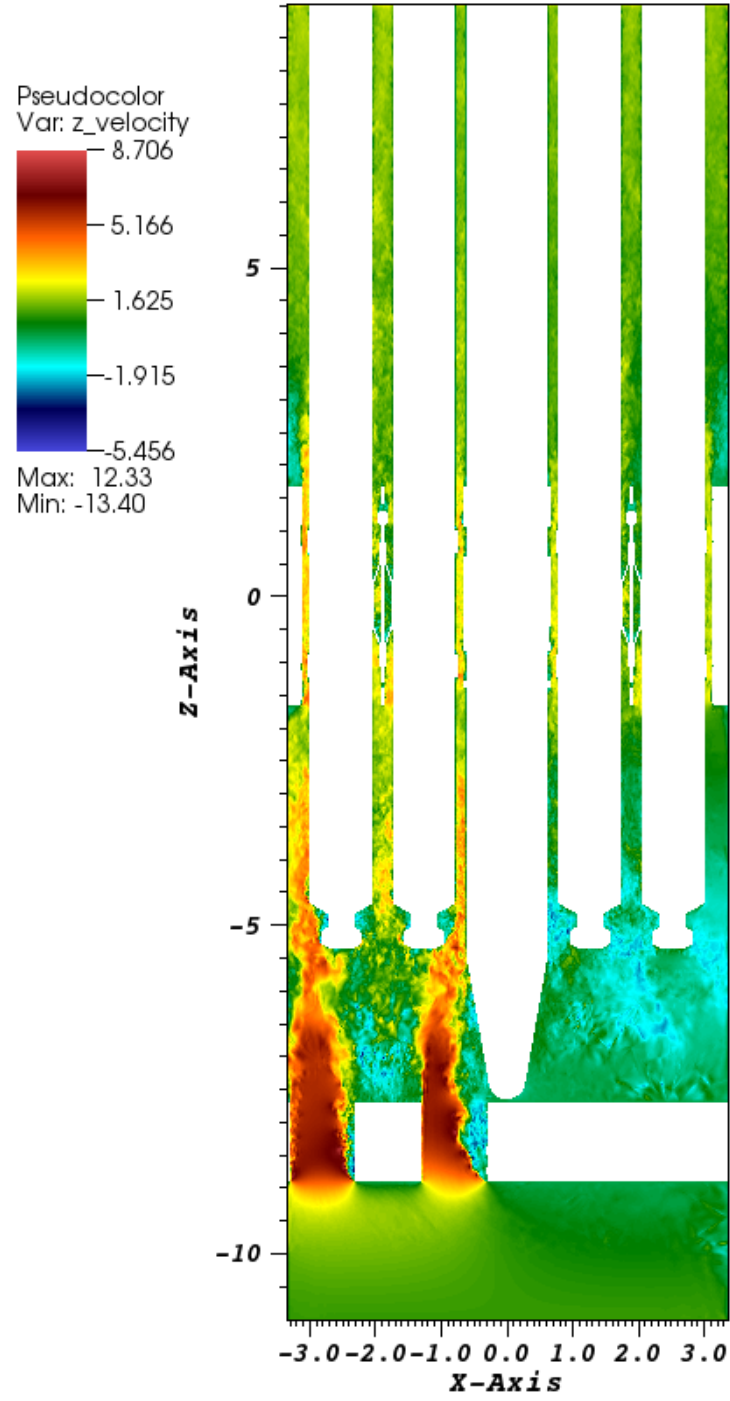


Figure 21: Vertical  $XZ$  profile of the instantaneous axial velocity flow field at  $y = 0$ . Unbalanced flow configuration with larger inlet holes on the left.

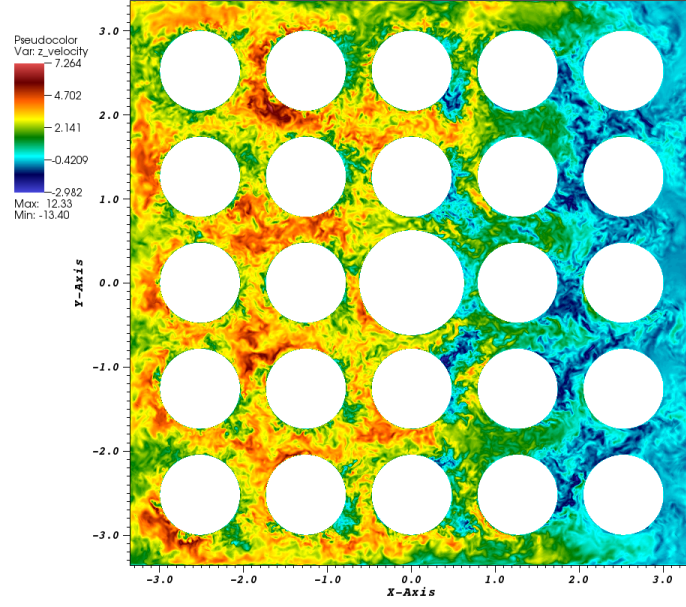


Figure 22: Horizontal  $XY$  profile of the instantaneous axial velocity flow field at H1.

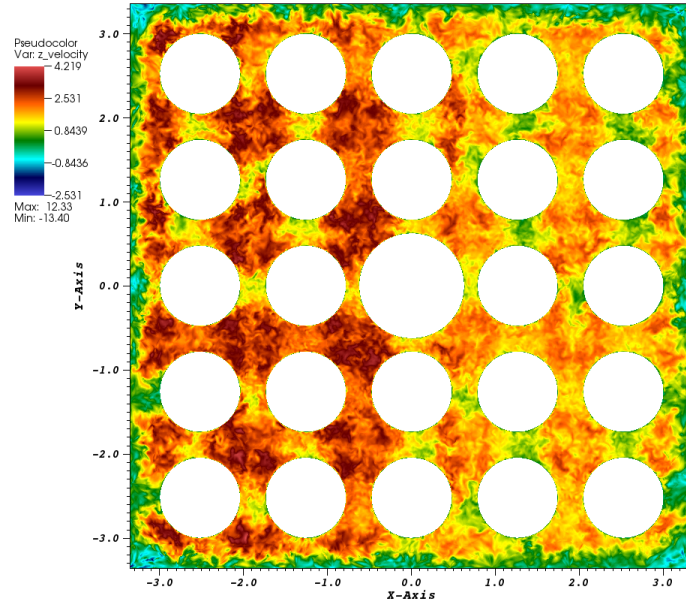


Figure 23: Horizontal  $XY$  profile of the instantaneous axial velocity flow field at N1.

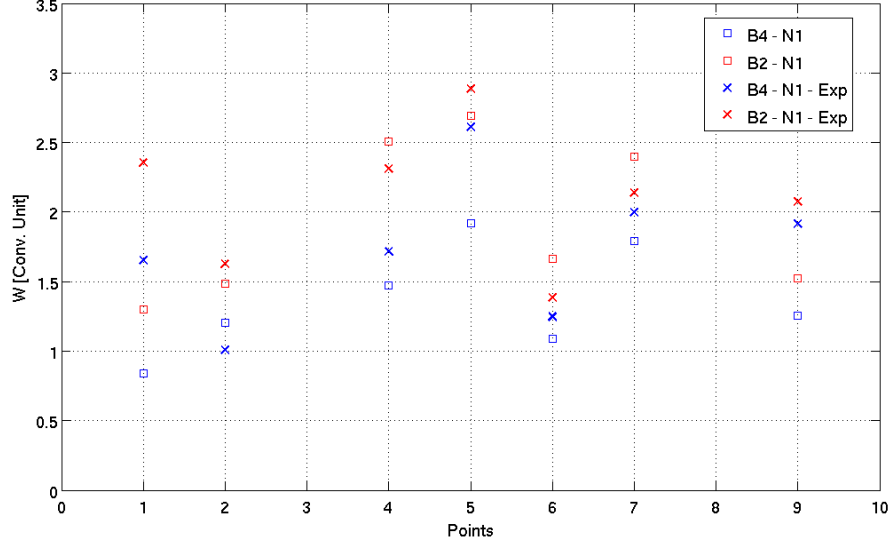


Figure 24: Simulation and experimental results of the time-averaged axial velocities at the points around the rods B2 and B4 at the elevation N1. The values are in convective units.

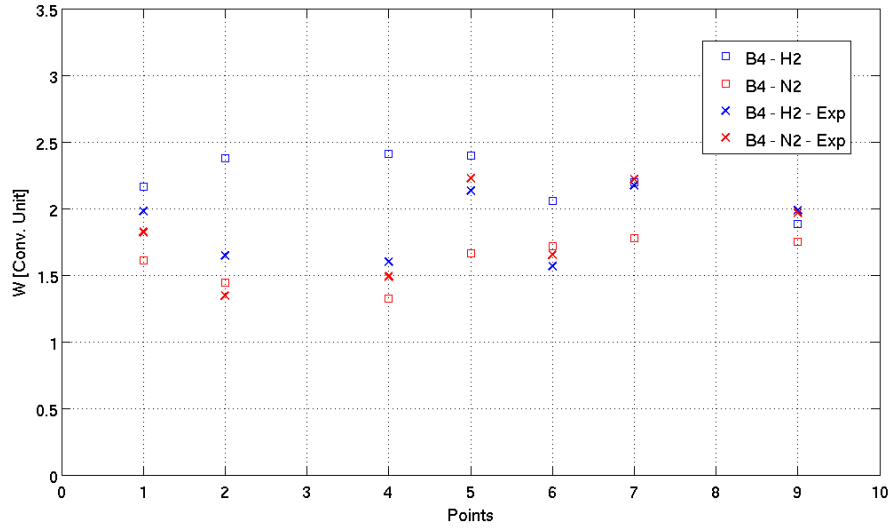


Figure 25: Simulation and experimental results of the time-averaged axial velocities at the points around the rod B4 at the planes H2 and N2. The values are in convective units.

Figure 26 shows the calculated turbulent intensity  $I_w$  (defined above) of the axial velocity component for the rods B2 and B4 at the plane N1 and compared with the experimental results. Given the insufficient collection of statistics, the points for the rod B4 (blue squares) still demonstrate satisfactory agreement with the experiment, except for point 4. However, results for the rod B2 (red squares) show much worse agreement for all seven points. This is consistent with the fact

that the rod B2 is on the side of the inlet holes and consequently the flow velocity on that side is considerably higher than for the rod B4 (see Figure 23). This makes the points around the rod B2 more sensitive to statistical noise.

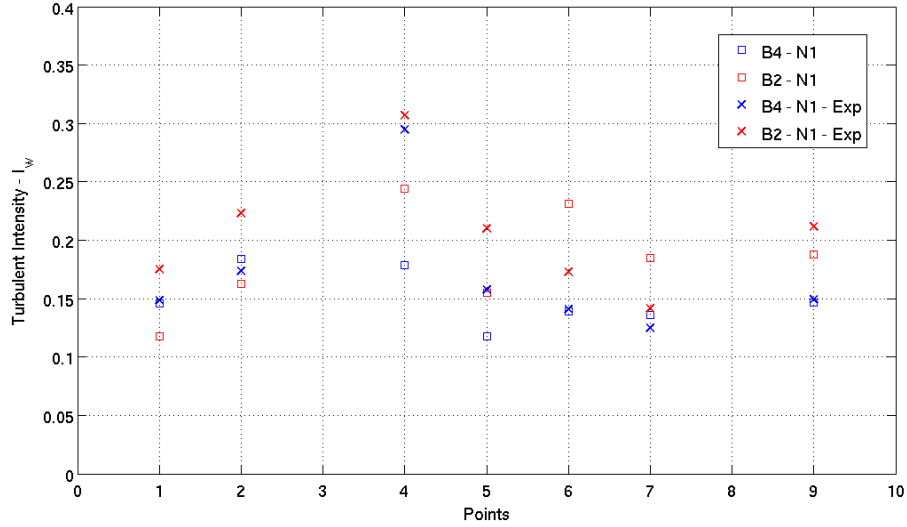


Figure 26: Axial turbulent intensity compared with experimental results. The data are for the points around the rods B2 and B4 at the elevation N1.

Turbulent length scales, autocorrelations, and Fourier spectra for the unbalanced flow were unreliable to calculate from the collected data. These calculations will be done as future work. We stress again that the results for the unbalanced case are preliminary and should be treated as such.

## 4 Conclusions

Nek5000 simulations were performed to model a turbulent coolant flow in a 5x5 fuel rod assembly for two flow configurations — balanced and unbalanced. The results were compared with the experimental data. The data for the balanced case were collected over 4 convective time units (33 ms of physical time), which allowed sufficient accumulation of statistics. The average axial velocities and turbulent intensities showed good agreement with the experimental measurements for most points at all four elevations. Exceptions were points 2 and 4, which were close to the B4 rod surface and therefore inherently hard to match precisely. Autocorrelations and Fourier spectra were also calculated for the balanced case. Even though the general trends of the curves matches the experimental observations, more data is necessary in order to resolve the low-frequency region.

The unbalanced case, on the other hand, is preliminary and lacks sufficient statistical convergence. It needs longer run times to generate more reliable data. The mesh for this case can also be improved, especially between the inlet holes and the fuel rods, in order to produce smoother velocity profiles. Despite these deficiencies, some simulation results (turbulent intensity for B4 at plane N1, Figure 26) demonstrate a reasonable match with the experimental data.

Overall, the results presented here represent an important stepping stone toward validation of the Nek5000 for simulating of the flow in fuel assemblies with grid spacers and the evaluation of fluid loads for FIV calculations. Given the complexity of the calculations and the flow involved, the work reported here represents one of the major milestones of the FIV work performed under the NEAMS program in the past three years.

## **Acknowledgments**

This material was based upon work supported by the U.S. Department of Energy, Office of Nuclear Energy, as part of the Nuclear Energy Advanced Modeling and Simulation (NEAMS) Program, under contract No. DE-AC02-06CH11357.

We thank Yiqi Yu from the Nuclear Engineering division for his help with the initial stages of the mesh development. This research used resources of the Argonne Leadership Computing Facility, which is a DOE Office of Science User Facility supported under Contract DE-AC02-06CH11357.

# Bibliography

- [1] Haomin Yuan, Jerome Solberg, Elia Merzari, Adam Kraus, and Iulian Grindeanu. Flow-induced vibration analysis of a helical coil steam generator experiment using large eddy simulation. *Nuclear Engineering and Design*, 322:547–562, 2017.
- [2] E. Merzari, H. Yuan, A. Kraus, J. Solberg, and R. M. Ferencz. Coupled calculations in helical steam generator: Validation on legacy data. Technical Report ANL/NE-16/49, Argonne National Laboratory, Lemont, IL (United States), 2016.
- [3] P. Fischer, J. Lottes, W.D. Pointer, and A. Siegel. Petascale algorithms for reactor hydrodynamics. *J. Phys. Conf. Series*, 125(1), 2008.
- [4] M.O. Deville, P.F. Fischer, and E.H. Mund. *High-Order Methods for Incompressible Fluid Flow*. Cambridge Monographs on Applied and Computational Mathematics. Cambridge University Press, 2002.
- [5] Paul F Fischer. An overlapping schwarz method for spectral element solution of the incompressible Navier-Stokes equations. *Journal of Computational Physics*, 133(1):84 – 101, 1997.
- [6] Paul F. Fischer and Anthony T. Patera. Parallel spectral element solution of the Stokes problem. *Journal of Computational Physics*, 92(2):380–421, 1991.
- [7] Y. Maday and A. T. Patera. Spectral element methods for the incompressible Navier-Stokes equations. In *State-of-the-Art Surveys on Computational Mechanics*, pages 71–143, 1989.
- [8] A. G. Tomboulides, J. C. Y. Lee, and S. A. Orszag. Numerical simulation of low Mach number reactive flows. *Journal of Scientific Computing*, 12(2):139–167, June 1997.
- [9] Ananias G. Tomboulides and Steven A. Orzag. A quasi-two-dimensional benchmark problem for low Mach number compressible codes. *Journal of Computational Physics*, 146(2):691–706, 1998.
- [10] S. Stolz, P. Schlatter, and L. Kleiser. High-pass filtered eddy-viscosity models for large-eddy simulations of transitional and turbulent flow. *Physics of Fluids*, 17(6), 2005.
- [11] J. Walker, E. Merzari, A. Obabko, P. Fischer, and A. Siegel. Accurate prediction of the wall shear stress in rod bundles with the spectral element method at high Reynolds numbers. *International Journal of Heat and Fluid Flow*, 50:287–299, 2014.

- [12] E. Merzari, P. Fischer, and W.D. Pointer. Numerical simulation and proper orthogonal decomposition of the flow in a counterflow T-junction. *Journal of Fluid Engineering*, 135:091304, 2013.
- [13] O. Pironneau, J. Liou, and T. Tezduyar. Characteristic-Galerkin and Galerkin/least-squares space-time formulations for the advection-diffusion equation with time-dependent domains. *Computer Methods in Applied Mechanics and Engineering*, 100(1):117–141, 1992.





**Mathematics and Computer Science Division**

Argonne National Laboratory

9700 South Cass Avenue, Bldg. 240

Lemont, IL 60439

[www.anl.gov](http://www.anl.gov)



Argonne National Laboratory is a U.S. Department of Energy  
laboratory managed by UChicago Argonne, LLC